Diffusion–Drift Modeling of a Growing Breast Cancerous Cell

Ahmed M. Hassan*, *Student Member, IEEE*, and Magda El-Shenawee, *Senior Member, IEEE*

***Abstract*—This paper presents a 2-D model to calculate the electric current densities and the biopotential differences generated due to a breast cancerous cell during the hyperpolarization of the G1/synthesis (G1/S) transition. The proposed model is based on semiconductor diffusion–drift analysis, and aims to understand the biophysics associated with growing breast cancerous cells. The effect of the duration of the G1/S transition, and the diffusivity and the mobility of the cancerous cell boundary is investigated. The results show that shorter G1/S transition durations, and higher diffusivity and mobility at the cell boundary provide higher magnitude of the electric signals.**

***Index Terms*—Bioelectric phenomena, biological cells, biophysics, cancer, MCF-7 cells.**

I. Introduction

THE COMPLEXITY of breast cancer detection has fueled extensive research in finding new detection modalities capable of discovering and treating breast tumors at early stages. Passive detection of breast cancer takes advantage of electromagnetic signals naturally produced by growing tumors, which has recently received increasing attention [1]–[7]. There are two main modalities for the passive electromagnetic detection of breast cancer: 1) *biomagnetic* [1]–[3] and 2) *biopotential* [4]–[7] detection. In passive biomagnetic detection of breast cancer, the magnetic field produced due to growing breast tumors was recorded using highly sensitive magnetometers termed super conducting quantum interference devices (SQUIDs) [1]–[3]. In passive biopotential diagnosis of breast cancer, two electrodes are employed: one electrode is placed on top of the breast lesions, and the second on a different part of the patient. Sensing natural electromagnetic signals could indicate to tumor activity, in the sense that, the more malignant the tumor grows, the higher the produced electromagnetic signals [1]–[7]. Passive biomagnetic and biopotential techniques are noninvasive with no exposure to any type of radiation.

The concept of biopotential and biomagnetic detection from adult brains as well as fetal brains where the signals are much weaker is well established [8], [9]. In this paper, we are trying to understand the biomagnetic and biopotential signals of a single breast cancerous cell. Understanding the biophysics of a single breast cancerous cell is vital for answering these questions. A biophysics-based model and computer simulations will be employed here to obtain the spatial and the temporal electric current densities, and the associated biopotentials produced by a single breast cancerous cell. These electric current densities can be integrated to calculate the biomagnetic fields produced by a cancerous lesion [10, eq. (4)].

Cancerous cells modulate their membrane potential during cell division [11]–[17]. A common pattern for a dividing cancerous cell is to decrease (depolarize) its membrane potential at the beginning of the G1 state followed by an increase in the membrane potential (hyperpolarization) in the G1/synthesis (G1/S) state transition [13], [14]. A standard breast cancer cell line, MCF-7, was found to hyperpolarize its membrane potential during the G1/S state transition by increasing the permeability of its membrane to potassium ions [15]–[17]. The numerical results of this paper are validated with these experimental data. In addition, the proposed paper aims to explain the macroscopic electric signals measured on or outside the breast based on these G1/S cellular activities.

The motivations for developing such a model are to provide a tool to understand the experimental measurements and prove that the growing tumor cells are indeed generating electric signals. The proposed model will be able to answer the question whether weak electromagnetic signals can propagate from the tissue near the tumor to the sensor positions outside the breast. The spatial and temporal distribution of the simulated electromagnetic signals can help in providing information regarding the optimum distribution of sensors around the breast, as suggested by Cuzick *et al.* in [7], but it is not in the scope of this paper.

In this paper, the electric current densities and biopotential variations associated with a growing breast tumor cell are calculated. In most models for cellular activity, the cell is assumed to exist in an infinite homogeneous medium with constant properties such as constant ion concentrations [18]. However, the proposed model avoids such simplification by placing the cell in a semifinite dynamic environment with realistic anatomical features such as a blood vessel and a tissue boundary. This allows the calculation of the spatial as well as the temporal variations in the electric signals.

Even though only a single cell is considered here, the analysis is challenging due to the fact that both the 2-D spatial as well as the temporal variations of the charged ion distributions need to be calculated. This means that the ion concentrations at each pixel and at each time step needs to be calculated, which can lead to extensive computational requirements. In addition, four nonlinear coupled differential equations are solved to describe

Manuscript received February 10, 2009; revised April 26, 2009. First published June 12, 2009; current version published September 16, 2009. This work was supported in part by the Doctoral Academy Fellowship at the University of Arkansas and in part by the National Science Foundation (NSF) under Award ECS-0524042. *Asterisk indicates corresponding author*.

*A. M. Hassan is with the Department of Electrical Engineering, University of Arkansas, Fayetteville, AR 72701 USA (e-mail: amhassan@uark.edu).

M. El-Shenawee is with the Department of Electrical Engineering, University of Arkansas, Fayetteville, AR 72701 USA (e-mail: magda@uark.edu).

Digital Object Identifier 10.1109/TBME.2009.2024539

the motion of the charged ions. Discretizing coupled nonlinear differential equations is, in general, not trivial, and needs to be performed with care to ensure stability and consistency [19]. Finally, techniques that realistically account for biological features, such as cell membranes, surrounding breast epithelia, ducts and tissue boundaries, need to be implemented [6], [7]. Such numerical challenges are overcome by correlating the similarities between the proposed biological model and the analysis of semiconductor electronic devices [19]–[21]. Therefore, the well-developed techniques for the analysis of semiconductor devices are adopted and utilized here to model the electric signals in cancerous cell.

For simplicity, the proposed model does not include all of ionic effects that occur in breast cancer cells. This proposed model represents the first step in our efforts to develop a more advanced model of electric signals in breast cancerous cells. Therefore, only four ions (potassium, sodium, chloride, and an ion representing the negatively charged proteins inside the cell) and two cellular processes (active transport and membrane permeability to ions) are considered here. These ions and processes have the largest impact on the cell membrane potential and internal ion concentrations [18]. In addition, they vary significantly during the process of cancerous cell division [13]–[17]. Although the proposed model considers only a single cell, it is feasible to advance the model to consider more than one cell that will be the topic of future work. The future model will incorporate cellular interactions, more nutrients, and tumor growth scheme.

Section II describes the biological foundation of the proposed model in detail. Section III describes the formulations of the model whereas Section IV shows the numerical results. Finally, Section V outlines the conclusion and future work.

II. Biophysical Foundation of the Model

It is well documented that there is a certain threshold (approximately -36 mV) for the membrane potential before cells can proliferate [12]. For example, muscle and nerve cells tend to have large membrane potentials that range from -70 to -90 mV, whereas dividing fibroblasts and embryos tend to have lower membrane potentials ranging from -10 to -30 mV [12]. Moreover, upon comparing the membrane potential of normal and cancerous proliferating cells from the same tissue, it was clearly evident that tumors exhibit lower magnitude membrane potential [12]. In order to reach this lower potential, cells need to regulate their internal ion concentrations. A hyperpolarization state usually follows the depolarization state such that the magnitude membrane potential of the cell returns to its original value. The proposed model simulates the aforementioned modulation of the membrane potential as the cell progresses through its life cycle.

Cancerous neuroblastoma cells' mechanisms of modulating the membrane potential were studied in detail in [13] and [14]. It was reported that membrane potential variations in the cell during division were attributed, in part, to changes in the cellular positive potassium ion concentration. Changes in the ion concentration during cell division were caused by two mechanisms: 1) changes in the absorption rate of potassium ion pumps in the cell membrane, which is an active process that consumes energy and 2) changes in the permeability of the cell membrane, which changes the amount of potassium ions crossing the membrane passively by diffusion [13], [14]. These two processes are incorporated in the proposed model.

More importantly, the experimental work of Wonderlin *et al.* [16] led to formulate a model in which potassium ion channel activity modulates cell growth in breast cancer cell line MCF-7 [15]. Wonderlin *et al.* focused the model on the transition between the G1 state and the S state. The G1 state is the state that follows mitosis and precedes the S state. The G1 state is a state of extensive cellular growth and protein synthesis, and it acts as the last checkpoint for the cell division. The S state is the state where the essential process of DNA replication is performed. In the model of Wonderlin *et al.*, the G1/S transition is accompanied by the opening of the potassium ion channels in the membrane that leads to the flow of potassium ions outside of the cell and the hyperpolarization of the membrane. Changes in the potassium ion channel activity in the membrane of cancerous cells were used to explain the elevated potential on the breast skin surface above the tumor [4]. The proposed model takes into account the time-varying channel activity through assigning time-varying diffusivity and mobility coefficients at the simulated cell boundary.

III. Formulations

The previously described cellular activities, active transport, and modulation of membrane potential lead to nonuniform distribution of charged ions [18]. These activities create diffusion forces trying to move the charged ions from regions of higher to regions of lower concentrations. Also, drift forces will be created that will move positive charges from higher to lower potentials, and negative charges in the opposite direction. The motion of charges will, in turn, modify the spatial potential distribution around the cell. The equations necessary to model the diffusion and drift effects are the Nernst–Plank, continuity and Poisson equations respectively [22], which are given as

$$\vec{J}_m = -D_m \nabla C_m - \mu_m C_m Z_m \nabla \varphi \tag{1}$$

$$\frac{\partial C_m}{\partial t} = -\vec{\nabla} \cdot \vec{J}_m \tag{2}$$

$$\nabla^2 \phi = -\frac{F}{\varepsilon} \sum_m Z_m C_m \tag{3}$$

where $\vec{J}_m$ is the flux or electric current density of ion *m* [in moles per (square centimeter·second], D_m is the diffusion coefficient of ion *m* (in square centimeters per second), C_m is the concentration of ion *m* (in moles per cubic centimeter), μ_m is the mobility of ion *m* [in square centimeters per (volt·second)], Z_m is the signed charge of ion *m*, φ is the electrostatic potential (in volts), *F* is Faraday's constant (96485 C/mol), and ε is the permittivity of the material (80 ε_0 for water under quasi-static conditions). Three ions, potassium C_{K^+}, sodium C_{Na^+}, and chloride C_{Cl^-} will be considered in this paper. These three ions play a major role in regulating the potential difference between the interior of

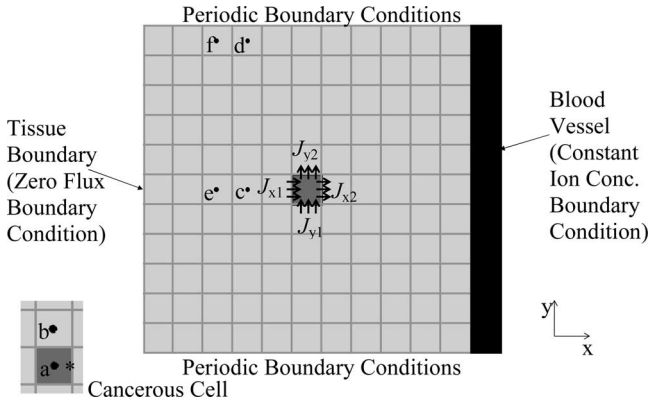

Fig. 1. Computational domain showing the blood vessel location (on right), a cancerous cell (dark gray), plasma (light gray), and the imposed boundary conditions. In all the subsequent results, $V_1 = \varphi_a - \varphi_b$, $V_2 = \varphi_c - \varphi_d$, and $V_3 = \varphi_e - \varphi_f$, where $\varphi_a, \varphi_b, \varphi_c, \varphi_d, \varphi_e$, and φ_f are the biopotentials at the points a, b, c, d, e, and f shown before.

TABLE I
SUMMARY OF PARAMETERS FOR BLOOD PLASMA†

Parameter	Description	Value
C_{K^+} C_{Na^+} C_{Cl^-}	The initial Potassium, Sodium and Chloride ion concentration respectively in all pixels. Also, these are the constant concentrations used for the blood pixels at all times	$C_{K^+} = 5mM$ $C_{Na^+} = 155mM$ $C_{Cl^-} = 160mM$
D_{K^+} D_{Na^+} D_{Cl^-}	The diffusion coefficients of Potassium, Sodium and Chloride ions, respectively, in plasma	$D_{K^+} = 1.96\times10^{-5}\ \frac{cm^2}{s}$ $D_{Na^+} = 1.33\times10^{-5}\ \frac{cm^2}{s}$ $D_{Cl^-} = 2.03\times10^{-5}\ \frac{cm^2}{s}$
u_{K^+} u_{Na^+} u_{Cl^-}	The mobility coefficients of Potassium, Sodium and Chloride ions respectively in plasma	$\mu_{K^+} = 7.62\times10^{-4}\,c\,\frac{cm^2}{sV}$ $\mu_{Na^+} = 5.19\times10^{-4}\ \frac{cm^2}{sV}$ $\mu_{Cl^-} = 7.92\times10^{-4}\ \frac{cm^2}{sV}$

†mM ≡ millimoles per litre, cm ≡ centimeter, s ≡ second, V ≡ volts. (R) indicates the values used in the reference state, (D) indicates the values used in the reference state, (H) indicates the values used in the hyperpolarization state. If not differentiated, then the same value was used in all three states.

the cell and its exterior, in addition to their abundance in either the intracellular or extracellular environment [18].

Fig. 1 shows the configuration that consists of a cancerous cell in plasma adjacent to a tissue boundary on the left and a blood vessel on the right. In spite of its simplicity, significant information can be achieved from this configuration following the work in several avascular tumor growth models [23]. However, angiogenesis, which is the tumor-induced blood vessel formation, is not considered in this model since the main goal is to investigate the electric signals induced by a tumor at an early state (when the tumor diameter is few millimeters) before angiogenesis starts to occur [24]. The cancerous cell is simulated such that its rate of active transport and membrane permeability resembles that of a realistic cancerous cell. Some of the parameters such as the diffusivity and mobility coefficients at the cell boundary (μb_m and Db_m) are unknown for MCF-7 cells. Therefore, we adopted values similar to those of the neuroblastoma cancerous cells, as will be discussed in Section III-B–E.

Equations (1)–(3) are discretized using the finite-difference scheme for the domain shown in Fig. 1. An $L \times L$ domain is used where L is chosen equal to 11 pixels. This value is selected since it provides a large separation between the cancerous cell and its y-boundaries. Preliminary results showed that the effect of the cell on the extracellular voltage was significant to about 3 pixels around the cell. Hence, 5 pixels are added on each side of the cell making $L = 11$. When a larger value was used, the electric signals remained unchanged, but the computational time increased. The spatial step Δ in the x- or y-direction is set equal to 10 μm, which is the average size of a human cell [25].

At the pixels corresponding to the blood vessel, nominal concentrations of ions are assigned that are unvaried with time throughout the simulations. Table I shows the values of all the parameters used in the model including the ion concentrations of the blood vessel, which are obtained from [25]. However, the concentration of chloride ions is slightly higher than that shown in [25], the blood has other negative ions that are not considered in this model. Therefore, to satisfy electrostatic neutrality, the chloride ion concentration is slightly increased. Table I also shows the diffusivity and mobility coefficient in plasma [26]. Since plasma is mostly water, the diffusivity and mobility coefficients in [26] for water are selected. Other parameters values will be discussed in later sections.

The simulated blood vessel contains a significant amount of ion concentrations, which is assumed constant here [23]. The resistivity of blood is lower than that of most other tissues [27]; therefore, the blood vessel is assumed to be an equipotential boundary. The potential values of the blood pixels are set equal to a reference zero. The left-hand side of the domain in Fig. 1 is assumed to be a generic tissue boundary where all the fluxes are set to zero (i.e., $\frac{\partial C_m}{\partial x} = 0$, $\frac{\partial \phi}{\partial x} = 0$). The top and bottom boundaries of the domain in Fig. 1 are assigned periodic boundary conditions such that the computational domain is repeated infinitely in the y-direction. This is achieved by setting $C_m(L+1, j) = C_m(2, j)$ and $\varphi(L+1, j) = \varphi(2, j)$ at the top boundary, and setting $C_m(0, j) = C_m(L-1, j)$ and $\varphi(0, j) = \varphi(L-1, j)$ at the bottom. Periodic boundary conditions are selected due to their extensive use in tumor growth models [23], [28], [29]. Periodic boundary conditions are adopted to extend the computational domain without adding more pixels to keep the computational time practical [28].

There are two main techniques for solving the finite-difference equations: *explicit* and *implicit* discretization. Discretizing the coupled Poisson and continuity equations using explicit and/or implicit schemes were implemented extensively

in semiconductors [19]–[21]. The explicit scheme requires the use of a very small time step Δ_t for the solution to be stable, almost 20–50 times smaller than that of the implicit scheme [19]. This leads to about 10–30 larger computational time required for the explicit scheme (due to additional complexity in the implicit scheme). Full-implicit discretization permits the use of larger time steps in comparison to explicit schemes, and hence, becomes more efficient [19]. Since biological processes usually occur over a long time, in the order of hours, the implicit scheme is selected here.

A. Implicit Discretization

The potential values ϕ^{t+1} at each pixel at the time step (t+1) are produced upon implicitly descretizing (3) as follows [19]:

$$\nabla^2\varphi^{t+1} = -\frac{F}{\varepsilon}\sum_m Z_m C_m^{t+1}. \tag{4}$$

The values of C_m^{t+1} are approximated using Taylor series as [19]

$$C_m^{t+1} = C_m^t + \Delta t\left(\frac{\partial C_m^t}{\partial t}\right) + \frac{\Delta t^2}{2}\left(\frac{\partial^2 C_m^t}{\partial t^2}\right)\cdots. \tag{5}$$

Upon retaining only the first two terms in (5) and using (2), C_m^{t+1} can be expressed as

$$C_m^{t+1} = C_m^t - \Delta t\cdot\left(\vec{\nabla}\cdot\vec{J}_m^{t,t+1}\right). \tag{6}$$

Substituting (6) in (4), the following is obtained:

$$\nabla^2\phi^{t+1} = -\frac{F}{\varepsilon}\sum_m Z_m\left(C_m^t - \Delta t\cdot\vec{\nabla}\cdot\vec{J}_m^{t,t+1}\right). \tag{7}$$

It is important to note that the ion concentrations C_m and the potential φ at any time step will be evaluated at the center of the pixel. The electric current density from one pixel to the adjacent, the diffusivity and the mobility coefficients will be evaluated at the boundary between two pixels. Equation (7) is then spatially discretized as follows:

$$\nabla^2\varphi^{t+1}(i,j) = \frac{\begin{pmatrix}\varphi^{t+1}(i+1,j)+\varphi^{t+1}(i-1,j)\\ +\varphi^{t+1}(i,j+1)+\varphi^{t+1}(i,j-1)\\ -4\varphi^{t+1}(i,j)\end{pmatrix}}{\Delta^2} \tag{8}$$

with

$$\vec{\nabla}\cdot\vec{J}_m^{t,t+1} = \left(J_{xm}(i,j+0.5) - J_{xm}(i,j-0.5)\right)/\Delta + \left(J_{ym}(i+0.5,j) - J_{ym}(i-0.5,j)\right)/\Delta \tag{9}$$

and

$$J_{xm}(i,j+0.5) = \frac{-D_m(i,j+0.5)\left(C_m^t(i,j+1) - C_m^t(i,j)\right)}{\Delta} - Z_m\mu_m(i,j+0.5)C_m^t(i,j+0.5) \times \frac{\left(\varphi^{t+1}(i,j+1) - \varphi^{t+1}(i,j)\right)}{\Delta} \tag{10}$$

and

$$J_{xm}(i,j-0.5) = \frac{-D_m(i,j-0.5)\left(C_m^t(i,j) - C_m^t(i,j-1)\right)}{\Delta} - Z_m\mu_m(i,j-0.5)C_m^t,(i,j-0.5) \times \frac{\left(\varphi^{t+1}(i,j) - \varphi^{t+1}(i,j-1)\right)}{\Delta} \tag{11}$$

where J_{xm} and J_{ym} are the x and y components, respectively, of the electric current density of ion m. Since the concentration values are only evaluated at integer multiples of i and j, $C_{m,}(i,j+0.5)$ is replaced by the average $(C_{m,}(i,j+1) + C_{m,}(i,j))/2$, and $C_{m,}(i,j-0.5)$ is replaced with the average $(C_{m,}(i,j) + C_{m,}(i,j-1))/2$. Similar expressions are used for $J_{ym}(i+0.5,j)$ and $J_{ym}(i-0.5,j)$. This will ensure the continuity equation at each pixel.

One of the advantages of the aforementioned model is that it assigns different mobility and diffusivity coefficients at different regions of the grid, thus allowing the modeling of different media. For example, the cell membrane of a living cell is semipermeable, and therefore, will not allow ions to flow as freely as in plasma [25]. If a living cell is located at pixel (i,j), the diffusivity (Db_m) and the mobility (μb_m) coefficients at the cell boundaries, $(i,j+0.5)$, $(i,j-0.5)$, $(i+0.5,j)$, and $(i-0.5,j)$, are set to a the values significantly smaller than their surroundings. Equation (7), using (8)–(11), is then solved for φ^{t+1} [30].

Similarly, (2) is discretized implicitly with respect to time to obtain

$$\frac{C_m^{t+1} - C_m^t}{\Delta t} = -\vec{\nabla}\cdot\vec{J}_m^{t+1} \tag{12}$$

where $\nabla\vec{J}_m^{t+1}$ is obtained from (9)–(11) upon replacing t by $t+1$ for all the ion concentrations values C_m^t. The potential values ϕ^{t+1} can be obtained from the solution of (7) leaving C_m^{t+1} to be the only unknown in (12) to be solved for.

B. Cancerous Cell Active Transport

A pixel bearing a living cell can exchange ions with its surroundings using active transport [25]. Active transport is performed by the cell membrane, and may occur in directions opposite to those of diffusion and drift forces. Equations (1)–(3) account for diffusion and drift forces, but not for the active transport. The sodium–potassium active pump, known as the (Na^+–K^+) ATPase pump, actively pumps potassium into the cell and sodium out of the cell consuming energy or ATP during the process. The (Na^+–K^+) ATPase pump is integrated in the model due to its presence in the membranes of almost all animal cells [25]. For a typical living cell at pixel *(i, j)*, the active influx is modeled as

$$C_m(i,j) = C_m(i,j) + f_m\Delta_t \tag{13a}$$

$$C_m(i,j) = \frac{C_m(i,j) - f_m\Delta_t}{4} \tag{13b}$$

where $I,J = (i,j-1),\ (i,j+1),\ (i-1,j),\ (i+1,j)$ represent the four immediate neighbors of the cell located at (i,j),

and the term f_m represents the rate of absorption for potassium ions and discharge for sodium ions in moles per (cubic centimeter·second). The equation for outflux can be obtained by reversing the sign of f_m in (13). Equation (13) is enforced at the end of each time step after all updates due to (1)–(3) are performed.

The (Na^+–K^+) ATPase pump injects three sodium ions out of the cell for two potassium ions each that it pumps into the cell [31]. The rate f_m of the ATPase pump is proportional to the intracellular sodium ion concentration and the extracellular potassium ion concentration while it is inversely proportional to the intracellular potassium ion concentration and the extracellular sodium ion concentration [31]. The pumping rate f_m for sodium ions (f_{Na^+}) and potassium ions (f_{K^+}) can be modeled as follows [31]:

$$f_{\mathrm{Na}^+} = -f_{\max} \times \left(\frac{C^t_{\mathrm{Na}^+\text{-i}}}{\left(C^t_{\mathrm{Na}^+\text{-i}} + K_{\mathrm{Na}^+\text{-i}}(1 + C^t_{\mathrm{K}^+\text{-i}}/K_{\mathrm{K}^+\text{-i}})\right)} \right)^3 \times \left(\frac{C^t_{K^+\text{-o}}}{\left(C^t_{\mathrm{K}^+\text{-o}} + K_{\mathrm{K}^+\text{-o}}(1 + C^t_{\mathrm{Na}^+\text{-o}}/K_{\mathrm{Na}^+\text{-o}})\right)} \right)^2 \tag{14a}$$

$$f_{K^+} = -0.667 f_{\mathrm{Na}^+} \tag{14b}$$

where $f_{\max}$ is the maximum pumping rate, $C^t_{\mathrm{Na}^+\text{-i}}$ and $C^t_{\mathrm{K}^+\text{-i}}$ refer to the intracellular sodium and potassium concentrations, respectively, and $C^t_{\mathrm{Na}^+\text{-o}}$ and $C^t_{\mathrm{K}^+\text{-o}}$ refer to the extracellular sodium and potassium concentrations, respectively. The $K_{\mathrm{Na}^+\text{-i}}$, $K_{\mathrm{K}^+\text{-o}}$, and $K_{\mathrm{Na}^+\text{-o}}$ factors are termed as *dissociation coefficients*. The values for these *dissociation coefficients* for the MCF-7 cells are, to the best of our knowledge, unknown. As an estimate, their values are set equal to those of red blood cells [31]. The numerical results in Section IV will justify this estimate. This estimate needs more investigation in the future. The magnitude of the active current (J_a) between the cell and its surroundings can be obtained using the continuity equation as follows:

$$J_a = \frac{-f_m \Delta}{4} \tag{15}$$

where Δ is the spatial discretization step, as explained in previous sections.

In the next section, the establishment of the reference state is described followed by the description of the depolarization state. Finally, Section IV-E describes how the hyperpolarization state is generated, which is the main focus of this paper.

C. C_{A^-}, $f_{\max}$, Db_m, and μb_m for the Reference State

Prior to modeling the hyperpolarization state, a reference state had to be set to describe the membrane potential of the cell before its division. Initially, all pixels in Fig. 1 are assigned an equal potential of zero and equal ion concentrations at the values shown in Table I. Three major parameters control the reference state: 1) the intracellular negative fixed charges (C_{A^-}); 2) the diffusion (Db_m) and mobility (μb_m) coefficients of the cell boundaries; and 3) the maximum pumping rate ($f_{\max}$) [18].

A fixed negative charge is added to the interior of the cell to account for the negatively charged intracellular proteins that cannot penetrate the cell boundary. The concentration of this fixed negative charge is set equal to 135 mM, which, in general, is comparable to the value of fixed negative charges in human cells [25].

The exact values of the diffusivity (Db_m) and mobility (μb_m) coefficients for the membranes of MCF-7 cells are unknown. Therefore, Db_m and μb_m are selected such that the effective permeability of the simulated cell is comparable with that measured in neuroblastoma cells [13], [14]. Moreover, two sets, case 1 and case 2, of Db_m and μb_m coefficients for the cell boundary for each ion are selected to study their impact on the electric signals, as shown in Table II.

Finally, an appropriate value for the maximum pumping rate $f_{\max}$ is selected to achieve the following two constraints at the reference state: realistic intracellular potassium concentration ($\sim$139 mM) and sodium concentration ($\sim$12 mM) [25], and a resting potential, which is the difference in potential between the inside and outside of the cell before it starts dividing, of approximately -45 mV, which is typical of MCF-7 cells [15]. Two different values for $f_{\max}$ are chosen, one for each case of Db_m and μb_m, to achieve these two constraints. The parameters are summarized in Table II. Fig. 2(a) shows the potential difference V_1 between the inside and the outside of the cell (see Fig. 1). Fig. 2(b) and (c) shows the variation in the intracellular and extracellular concentrations of the three previously described ions, C_{K^+}, C_{Na^+}, and C_{Cl^-} versus the time. Fig. 2(a)–(c) shows the three states: reference, depolarization, and hyperpolarization.

In the reference state, the potential difference (V_1) changed from an initial value of zero to -42.3 mV, which is in agreement with the measured -45 mV [15]. The intracellular concentration C_{K^+} increased from an initial value of 5 to 136 mM, while the intracellular concentration C_{Na^+} decreased from an initial value of 155 to 15 mM. This is also in agreement with the values of 139 and 12 mM reported for C_{K^+} and C_{Na^+}, respectively, as shown in [25]. As for the C_{Cl^-}, it decreased from an initial value of 160 to $\sim$16 mM. This is higher than the value in normal human cells [25]. This is also due to the fact that other negative ions, such as hydrogen carbonate HCO_3^- ions, were not included in the model. The variations in the extracellular ion concentrations shown in Fig. 3(c) are not significant due to the small impact of a single cell on its surroundings.

D. C_{A^-}, $f_{\max}$, Db_m, and μb_m for the Depolarization State

In this paper, we use three ions (potassium, sodium, and chloride). However, potassium is the ion which plays the main role in regulating the membrane potential of MCF-7 cells [15]–[17]. In this state, the cell depolarization is enforced numerically by abruptly decreasing $f_{\max}$, and the Db_m and μb_m coefficients of potassium ions at the cell boundaries. The $f_{\max}$ parameter is reduced by 75% that was observed in other cancerous cells such as neuroblastoma cells [13], [14]. The Db_m and μb_m parameters at the cell boundaries are also simultaneously reduced by 90% of

TABLE II
SUMMARY OF PARAMETERS FOR CANCEROUS CELL IN THREE STAGES: REFERENCE (R), DEPOLARIZATION (D), AND HYPERPOLARIZATION (H)†

Case	Parameter	Description	Value
1 & 2	C_{A^-}	The concentration of the impermeable negatively charged proteins inside the cell	$135\,mM$
1	Db_{K^+} Db_{Na^+} Db_{Cl^-}	The diffusion coefficients (Db_m††) of Potassium, Sodium and Chloride ions respectively at the cell boundary	Db_{K^+} = 7.84 (R), 0.784 (D), 7.48(H) Db_{Na^+} = 0.665 Db_{Cl^-} = 3.25 ($\times 10^{-9}\ cm^2 s^{-1}$) for all values in this cell
1	ub_{K^+} ub_{Na^+} ub_{Cl^-}	The mobility coefficients (μb_m††) of Potassium, Sodium and Chloride ions respectively at the cell boundary	ub_{K^+} = 3.03 (R), 0.303 (D), 3.03(H) ub_{Na^+} = 0.257 ub_{Cl^-} = 1.255 ($\times 10^{-7}\ cm^2 s^{-1} V^{-1}$) for all values in this cell
1	f_{max}	Maximum pumping rate of the (Na^+-K^+) ATPase pump	f_{max} = 2 (R), 0.5 (D), 2 (H) (mMs^{-1}) for all values in this cell
2	Db_{K^+} Db_{Na^+} Db_{Cl^-}	The diffusion coefficients (Db_m††) of Potassium, Sodium and Chloride ion respectively at the cell boundary	Db_{K^+} = 0.784 (R), 0.0784 (D), 0.748(H) Db_{Na^+} = 0.0665 Db_{Cl^-} = 0.325 ($\times 10^{-9}\ cm^2 s^{-1}$) for all values in this cell
2	ub_{K^+} ub_{Na^+} ub_{Cl^-}	The mobility coefficients (μb_m††) of Potassium, Sodium and Chloride ions respectively at the cell boundary	ub_{K^+} = 0.3 (R), 0.03 (D), 0.3(H) ub_{Na^+} = 0.0257 ub_{Cl^-} = 0.1255 ($\times 10^{-7}\ cm^2 s^{-1} V^{-1}$) for all values in this cell
2	f_{max}	Maximum pumping rate of the (Na^+-K^+) ATPase pump	f_{max} = 0.2 (R), 0.05 (D), 0.2 (H) (mMs^{-1})for all values in this cell

†(R) indicates the values used in the reference state, (D) indicates the values used in the reference state, (H) indicates the values used in the hyperpolarization state. If not mentioned, it implies that the same is used in R, D, H states. Note the values indicated for the hyperpolarization state in Table II are the final values achieved at the end of the transitions shown in Fig. 3.†† Indicates boundary of the cell.

the reference values shown in Table II due to the 90% reduction in the MCF-7 permeability during the depolarization state [16]. The depolarization state results are also shown in Fig. 2(a) and (b). The V_1 results show a change from -42.3 mV in the reference state to approximately -15 mV, while it is approximately -10 mV in [15]. In Fig. 2(b), the C_{K^+} inside the cell decreased, and both the C_{Na^+} and C_{Cl^-} concentrations increased during the depolarization state.

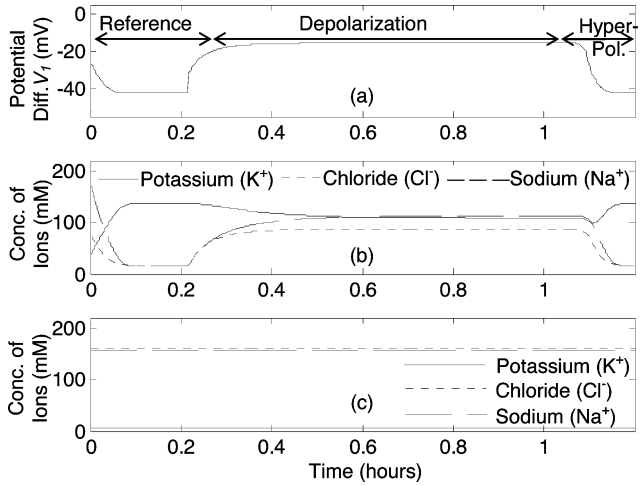

Fig. 2. (a) Variation of potential difference between the cell and its surroundings versus time. (b) Time variation of ion concentration inside the cell ($C^t_{Na^+\text{-i}}$, $C^t_{K^+\text{-i}}$, and $C^t_{Cl^-\text{-i}}$). (c) Time variation of ion concentrations outside the cell ($C^t_{Na^+\text{-o}}$, $C^t_{K^+\text{-o}}$, and $C^t_{Cl^-\text{-o}}$).

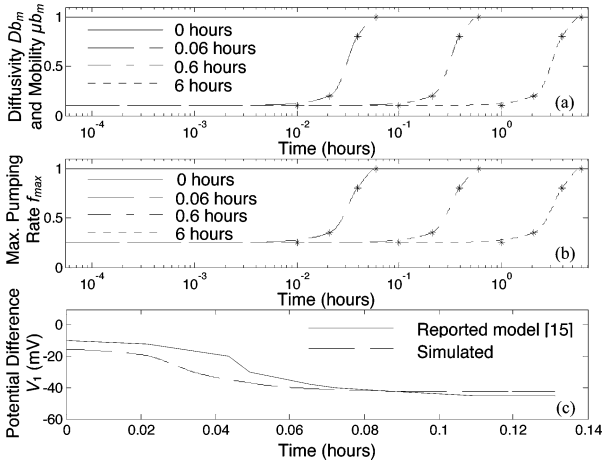

Fig. 3. (a) Hyperpolarization state time change in the normalized Db_m and μb_m of potassium ions in the cell boundaries. (b) Hyperpolarization state time change in the normalized $f_{\max}$. The $(*)$ indicate to the four points used in cubic interpolation. (c) Hyperpolarization state: a comparison between the simulated and reported potential difference between the inside and the outside of the cell (V_1).

E. C_{A^-}, $f_{\max}$, Db_m, and μb_m for the Hyperpolarization State

Finally, during the hyperpolarization state, the Db_m and μb_m coefficients of potassium ions are increased ten times of the values used in the depolarization phase, as shown in Table II. This ten-time increase is obtained from the experimental measurements of the MCF-7 cells [16]. Since, to the best of our knowledge, the variation in the pumping rate of MCF-7 cells during the hyperpolarization phase is unknown, the maximum pumping rate $f_{\max}$ will be increased back to its reference value

that is comparable to the increase exhibited in other cancerous cells [13], [14].

In the model in [15], the time of the hyperpolarization state was not specified. Therefore, four different time profiles that describe the increase in Db_m and μb_m are examined here. The goal is to investigate the effect of a variety of time durations of the G1/S transition on the electric signals. Note that Db_m, μb_m, and $f_{\max}$ in the depolarization state changed instantaneously (i.e., decreased suddenly, as shown in the example in case 1 in the fourth row of Table II, where $f_{\max}$ dropped from 2 mM·s^{-1} in the reference state to 0.2 mM·s^{-1} in the depolarization state). On the other hand, in the hyperpolarization state, the changes follow a certain time profile, as shown in Fig. 3(a) and (b).

Fig. 3(a) and (b) shows four different time profiles utilized in this model. Four different durations of the transitions, 0, 0.06, 0.6, and 6 h, are investigated in the four profiles. The profiles in Fig. 3(a) and (b) are obtained using cubical interpolation based on four selections of Db_m, μb_m, and $f_{\max}$ (marked as $*$). These four time profiles demonstrate a slow rate of change at the beginning, a sharp transition in the middle, and a slow rate of change at the end following the potential profile in [15], which investigated a model of the MCF-7 cell.

Fig. 3(c) shows a comparison between the current model and that of [15]. The potential difference is simulated using the parameters for case 1 in Table II, and the 0.06 h duration in Fig. 3(a) and (b). Fig. 3(c) demonstrates the validity of profiles in Fig. 3 in comparison with the model in [15]. Other simulations of V_1 showing the same trends were obtained using the parameters of case 1 and case 2, and the 0, 0.06, 0.6, and 6 h profiles transitions, as will be discussed in Section IV.

IV. Numerical Results

The numerical results of this section aim to show the evolution of electric current densities and biopotentials during the hyperpolarization state of an MCF-7 cancerous cell. The electric current densities to be presented here include both the active and passive parts. The passive parts of the electric current densities are calculated using (10) and (11). These two equations depend on ion concentrations C_{K^+}, C_{Na^+}, C_{Cl^-}, which are obtained using (1)–(9).

A. Adopted Model for Active Electric Current Density

The active part of the electric current density will be calculated using the adopted model of red blood cells [31]. This model is represented in (14) to calculate f_{Na^+} and f_{K^+} to be used in (15) to calculate the active part of the electric current density. The parameters $C^t_{\mathrm{Na}^+\text{-i}}$, $C^t_{\mathrm{K}^+\text{-i}}$, $C^t_{\mathrm{Na}^+\text{-o}}$, and $C^t_{\mathrm{K}^+\text{-o}}$ are obtained at each time step from Fig. 2(b) and (c), respectively, and are associated with the MCF-7 cancerous cell. The differences in the ion concentrations $C^t_{\mathrm{Na}^+\text{-o}}$ and $C^t_{\mathrm{K}^+\text{-o}}$ outside the cell are not significant due to the small impact of a single cell on its surroundings. The exact values of $K_{\mathrm{Na}^+\text{-i}}$, $K_{\mathrm{K}^+\text{-i}}$, $K_{\mathrm{K}^+\text{-o}}$, and $K_{\mathrm{Na}^+\text{-o}}$ are not known for MCF-7 cells; therefore, we adopt the same values in [31].

Fig. 4 presents the passive and active parts of the electric current density, respectively, at the cell boundary. Results in

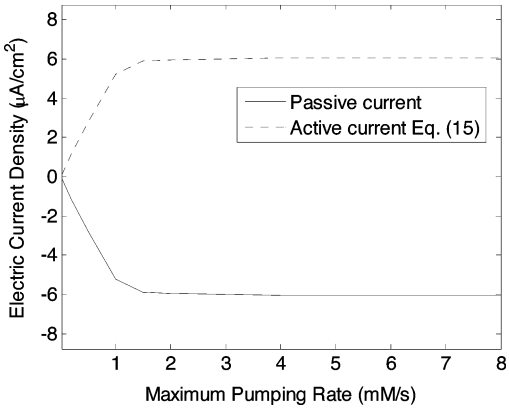

Fig. 4. Variation of the passive and active currents versus different pumping rates.

Fig. 4 are presented by only using case 1 coefficients at steady state at the end of the reference state. The results show that as $f_{\max}$ increases, the passive and active currents both increase almost linearly up to $f_{\max} = 1$ mM/s where the current densities become $= 5.2$ μA/cm^2. Beyond this point, the electric current density becomes almost constant since the intracellular sodium ion concentration $C^t_{\mathrm{Na}^+\text{-i}}$ drops, which counters the increase in $f_{\max}$, as shown in (14).

The significance of Fig. 4 is to show that the passive and active parts of the electric current density are equal as expected [18]. Other formulas for f_m (e.g., $f_m = f_{\max}$) were tested, and the results show the same equality of the two currents at steady state (not presented here). Case 2 coefficients showed the same equality (not presented here).

In the remainder of this section, the model of [31] is adopted for the active electric current density even though the values of $K_{\mathrm{Na}^+\text{-i}}$, $K_{\mathrm{K}^+\text{-i}}$, $K_{\mathrm{K}^+\text{-o}}$, and $K_{\mathrm{Na}^+\text{-o}}$ associated with red blood cells and not with MCF-7 cancerous cells are used. The results of Fig. 4 give confidence that the proposed model of the electric current densities is realistic.

B. Biopotentials V_1, V_2, and V_3 in the Hyperpolarization State

The potential difference V_1, as marked in Fig. 1, is calculated and shown in Fig. 6 ($V_1 = \phi_a - \phi_b$) . The plots (1a)–(1d) and (2a)–(2d) correspond to the coefficients of case 1 and case 2 in Table II, respectively. Plots a–d correspond to the four time profiles shown in Fig. 3.

The variation in the potential difference V_1 is plotted in Fig. 5. The results of Fig. 5(1a) and (2a) correspond to the 0-h profile of $f_{\max}, Db_m$, and μb_m in Fig. 3. Note the jump in V_1 from -15.5 to -30 mV at 0 time as expected due to the sudden jump in $f_{\max}, Db_m$, and μb_m in Fig. 3. For case 1 results, steady state is reached after $\approx$0.1 h, and after $\approx$1 h in case 2. This is due to the lower values of Db_m and μb_m in Table II that lead to slower response in case 2 as compared with case 1. Fig. 6(1b) shows that V_1 changes slowly in the beginning, is faster in the middle, and finally, converges to a steady state. Fig. 5(2b), on the other side, shows a sharper drop in the potential from -15.5 to approximately -30 mV resembling the results in (1a) and (1b). This is due to the low values of Db_m and μb_m in case 2

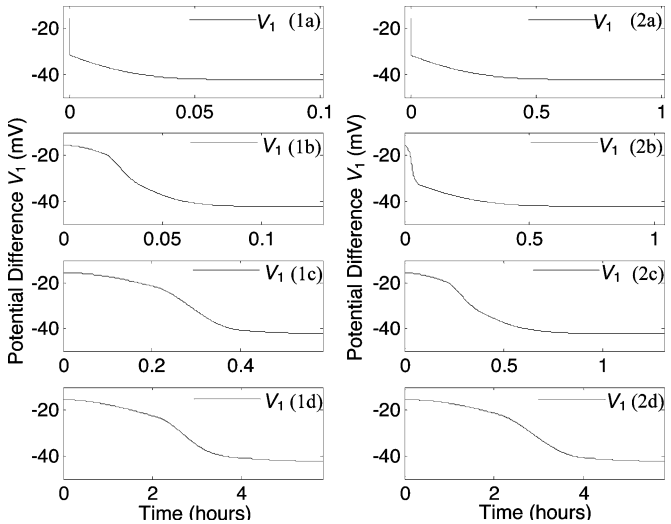

Fig. 5. Variation of V_1 during the hyperpolarization state for the two cases, each for the four profiles, in Fig. 3. Plots (1a)–(1d) correspond to case 1 and plots (2a)–(2d) correspond to case 2.

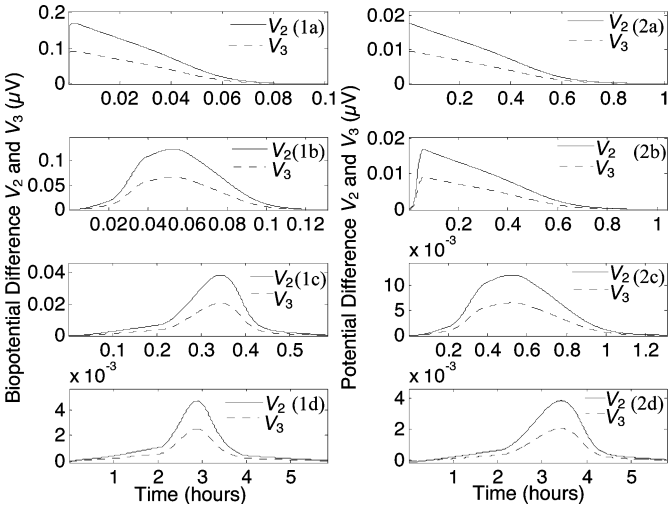

Fig. 6. Variation in V_2 (solid) and V_3 (dotted) during the hyperpolarization state for the two cases each for the four profiles in Fig. 3. Plots (1a)–(1d) correspond to case 1 and plots (2a)–(2d) correspond to case 2.

compared with those in case 1. The remaining results in Fig. 5 (case 1 or case 2) follow the aforementioned behavior, but with slower rates before reaching the steady state.

The results in Fig. 5 exhibit a behavior similar to the MCF-7 hyperpolarization state in [15] and shown in Fig. 3(c). In Fig. 5, V_1 changes from approximately -15 to approximately -42.3 mV at the end, which is in agreement with [15].

In biopotential detection of breast cancer, one electrode is placed on the breast above the tumor and another electrode is placed away from the tumor [4]–[7]. Therefore, potential differences, V_2 ($\phi_c - \phi_d$) and V_3 ($\phi_e - \phi_f$), indicated in Fig. 1 are shown in Fig. 6. Fig. 1 shows that V_2 is closer to the cell than V_3. In Fig. 7(1a) and (2a), V_2 changes instantaneously from 0 to 0.16 and 0.016 μV, respectively, whereas, V_3 changes from 0 to 0.09 and 0.009 μV, respectively. In Fig. 6(b)–(d), V_2 and V_3 gradually increase from zero to reach maximum values around

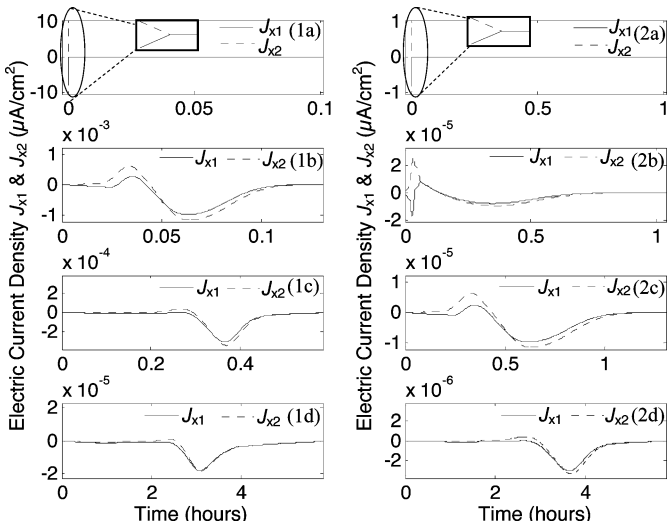

Fig. 7. Variation in J_{x1} (solid) and J_{x2} (dashed) during the hyperpolarization state for the two cases each for the four profiles in Fig. 3. Plots (1a)–(1d) correspond to case 1 and plots (2a)–(2d) correspond to case 2.

the middle of the transition in Fig. 3. In addition, in Fig. 6(a)–(d), V_2 and V_3 decay to zero at the end of the hyperpolarization state. Upon comparing Fig. 6(1b) with (2b), the results show a sharper jump in the potential due to the low values of Db_m and μb_m in case 2 compared with those in case 1.

Upon comparing the plots in Fig. 6(1a)–(1d), it can be shown that the maximum magnitudes of V_2 and V_3 decrease. For example, moving down from Fig. 6(1a) to (1d), the maximum of V_2 drops from 0.17 to 0.00473 μV. The same observation is shown in Fig. 6(2a)–(2d). The potential values V_2 and V_3 have larger maxima when the rate of change is fast or the G1/S transition is short. This is also indicated by the fact that the maxima of V_2 and V_3 in all eight cases in Fig. 6 are at the middle of the transition period. This is the phase where the slope of the Db_m, μb_m, and $f_{\max}$ profile is maximum. Upon comparing Fig. 6(1a)–(1d) with Fig. 6(2a)–(2d), it can be seen that V_2 and V_3 produced in case 1 are higher than those in case 2, suggesting that higher Db_m and μb_m lead to higher V_2 and V_3.

Experimental measurements show that the tumor site is found to be more positive [4]–[7]. The results in Fig. 6 are in agreement with these measurements since V_2 and V_3 are positive. Note also that V_2 is higher than V_3 since it has higher cell proximity.

C. Electric Current Densities J_{x1}, J_{x2}, J_{y1}, and J_{y2} in the Hyperpolarization State

The electric current densities, J_{x1} and J_{x2}, produced in the hyperpolarization state are plotted in Fig 7, and the electric current densities, J_{y1} and J_{y2}, are plotted in Fig 8. These currents represent the total current (active + passive) for the three ions at the cell boundary. The total current is the prime concern of this section due to its contribution to the biomagnetic fields. The plots (1a)–(1d) and (2a)–(2d) correspond to the coefficients of cases 1 and 2 in Table II, respectively. Plots a–d correspond to the four time profiles shown in Fig. 3(a) and (b).

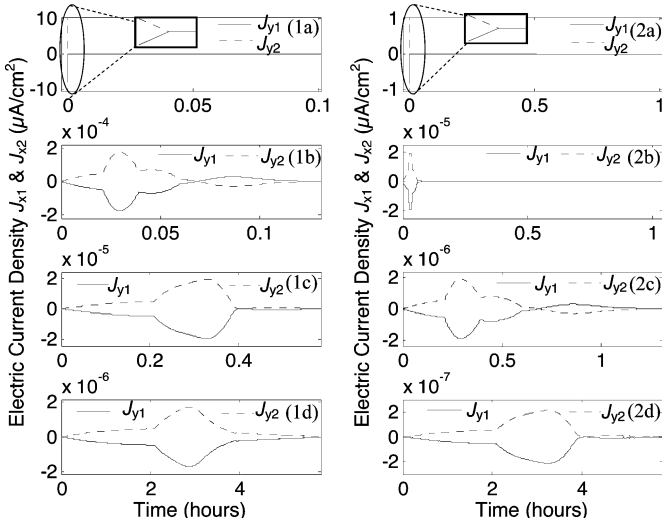

Fig. 8. Variation in J_{y1} (solid) and J_{y2} (dashed) during the hyperpolarization state for the two cases each for the four profiles in Fig. 3. Plots (1a)–(1d) correspond to case 1 and plots (2a)–(2d) correspond to case 2.

The results show that the electric current densities J_{x1} and J_{x2} are not symmetric due to the asymmetry in the *x*-direction caused by the presence of a tissue boundary on the left side and the presence of a blood vessel on the right side. This indicates to the important impact of anatomical features on electric signals produced by cancerous cell. Since the model is completely symmetric in the *y*-direction, J_{y1} and J_{y2} shown in Fig. 8 are identical, differing only in their sign. Upon zooming on Fig. 7(1a) and (2a), it can be shown that J_{x1} and J_{x2} drop from a maximum magnitude of 8 μA/cm^2 in case 1 and 0.84 μA/cm^2 in case 2 to approximately zero within 0.2 s. This is due to the sudden jump in $f_{\max}$, Db_m, and μb_m shown in the first profile in Fig. 3.

Similar to the results of the potential in Figs. 5 and 6, the results in Figs. 7 and 8 show that the maximum magnitudes of J_{x1}, J_{x2}, J_{y1}, and J_{y2} decrease upon comparing Fig. 7(1a)–(1d) and 8(1a)–(1d) for case 1. The same observation is shown in Figs. 7(2a)–(2d) and 8(2a)–(2d) for case 2. These observations indicate that the electric current densities have larger maxima when the rate of change is fast or when the G1/S transition is short. Upon comparing Figs. 7(1a)–(1d) and 8(1a)–(1d) with Figs. 7(2a)–(2d) and 8(2a)–(2d), it can be seen that J_{x1}, J_{x2}, J_{y1}, and J_{y2} produced in case 1 are higher than those in case 2, suggesting that the higher Db_m and μb_m lead to higher electric current densities similar to the potential results in Figs. 5 and 6.

V. Conclusion

The electric signals due to a single cancerous tumor cell during its G1/S state transition are simulated. The proposed model allows the calculation of *spatial* signals, such as the potential differences, in the surroundings of the cancerous cell. Upon calculating the spatial distribution of the electric signals, the maximum distance between the sensor and the tumor can be estimated in a future work. The results show that the cancerous cell can produce electric signals proportional to how fast the cell divides. This shows a potential for detection of fast dividing cells at an early stage. In addition, the results show that the high diffusivity and the mobility values at the boundary of the cancerous cell produce larger electric signals. The proposed model helps to understand the biophysics associated with growing breast cancerous cells that can aid in the development of new passive detection and treatment techniques. More ions, cell-to-cell interactions, and other cell division states need to be covered in a future work. Future development of this research will include coupling the model with a tumor growth model to produce the electric signals due to a whole tumor. This will help in calculating the biomagnetic fields using the electric current densities.

References

[1] Ph. A. Anninos, A. Kotini, N. Koutlaki, A. Adamopouos, G. Galazios, and P. Anastasiadis, "Differential diagnosis of breast lesions by use of biomagnetic activity and non-linear analysis," *Eur. J. Gynaecol. Oncol.*, vol. 21, no. 6, pp. 591–595, 2000.

[2] A. Kotini, A. Anastasiadis, N. Koutlaki, D. Tamiolakis, P. Anninos, and P. Anastiadis, "Biomagnetism in gynecologic oncology. Our experience in Greece," *Eur. J. Gynaecol. Oncol.*, vol. 27, no. 6, pp. 594–596, 2006.

[3] A. Hassan, M. El-Shenawee, and H. Eswaran, "A feasibility study for passive detection of breast tumors using naturally generated magnetic fields," presented at the IEEE AP-S Symp. USNC/URSI Nat. Radio Sci. Meeting, San Diego, CA, Jul. 2008, pp. 5–12.

[4] A. Marino, D. Morris, M. Schwalke, I. Iliev, and S. Rogers, "Electrical potential measurements in human breast cancer and benign lesions," *Tumor Biol.*, vol. 15, pp. 147–152, 1994.

[5] M. Faupel, D. Vanel, V. Barth, R. Davies, I. S. Fentiman, R. Holland, J. L. Lamarque, V. Sacchini, and I. Schreer, "Electropotential evaluation as a new technique for diagnosing breast lesions," *Eur. J. Radiol.*, vol. 24, no. 1, pp. 33–38, Jan. 1997.

[6] V. Sacchini, "Report of the European school of oncology task force on electropotentials in the clinical assessment of neoplasia," *Breast*, vol. 5, pp. 282–286, 1996.

[7] J. Cuzick, R. Holland, V. Barth, R. Davies, M. Faupel, I. Fentiman, H. Frischbier, J. LaMarque, M. Merson, V. Sacchini, D. Vanel, and U. Veronesi, "Electropotential measurements as a new diagnostic modality for breast cancer," *Lancet*, vol. 352, pp. 359–363, Aug. 1998.

[8] S. Baillet, J. Mosher, and R. Leahy, "Electromagnetic brain mapping," *IEEE Signal Process. Mag.*, vol. 18, no. 6, pp. 14–30, Nov. 2001.

[9] J. Vrba, S. E. Robinson, J. McCubbin, C. L. Lowery, H. Eswaran, P. Murphy, and H. Preissl, "Searching for the best model: Ambiguity of inverse solutions and application to fetal magnetoencephalography," *J. Phys. Med. Biol.*, vol. 52, pp. 757–776, Jan. 2007.

[10] J. Sarvas, "Basic mathematical and electromagnetic concepts of the biomagnetic inverse problem," *Phys. Med. Biol.*, vol. 32, pp. 11–22, 1987.

[11] M. Levin, "Bioelectromagnetics in morphogenesis," *Bioelectromagnetics*, vol. 24, pp. 295–315, 2003.

[12] R. Bingelli and R. Weinstein, "Membrane potentials and sodium channels: Hypothesis for growth regulation and cancer formation based on changes in sodium channels and gap junctions," *J. Theor. Biol.*, vol. 123, pp. 377–401, 1986.

[13] C. Mummery, J. Boonstra, L. Tertoolen, P. Van Der Saag, and S. De Laat, "Modulation of functional and optimal (Na+–K+)ATPase activity during the cell cycle of neuroblastoma cells," *J. Cell. Physiol.*, vol. 107, no. 1, pp. 1–9, 1981.

[14] J. Boonstra, C. Mummery, L. Tertoolen, P. Van Der Saag, and S. De Laat, "Cation transport and growth regulation in neuroblastoma cells. Modulations of K+ transport and electrical membrane properties during the cell cycle," *J. Cell. Physiol.*, vol. 107, no. 1, pp. 75–83, 1981.

[15] J. Strobl, W. Wonderlin, and D. Flynn, "Mitogenic signal transduction in human breast cancer cells," *Gen. Pharmacol.*, vol. 26, no. 8, pp. 1643–1649, 1995.

[16] W. Wonderlin, K. Woodfork, and J. Strobl, "Changes in membrane potential during the progression of MCF-7 human mammary tumor cells through the cell cycle," *J. Cell. Physiol.*, vol. 165, pp. 177–185, 1995.

[17] H. Ahidouch and A. Ahidouch, "K+ channel expression in human breast cancer cells: Involvement in cell cycle regulation and carcinogenesis," *J. Membr. Biol.*, vol. 221, pp. 1–6, 2008.
[18] J. Enderle, S. Blanchard, and J. Bronzino, *Introduction to Biomedical Engineering*, 2nd ed. New York: Elsevier/Academic, 2005.
[19] S. Yoganathan and S. Banerjee, "A new decoupled algorithm for non-staionary, transient simulations of GaAs MOSFET's," *IEEE Trans. Electron Devices*, vol. 39, no. 7, pp. 1578–1587, Jul. 1992.
[20] D. L. Scharfetter and H. K. Gummel, "Large-signal analysis of a silicon read diode oscillator," *IEEE Trans. Electron Devices*, vol. ED-16, no. 1, pp. 64–77, Jan. 1969.
[21] J. Kreskovsky, "A hybrid central difference scheme for solid-state device simulation," *IEEE Trans. Electron Devices*, vol. 34, no. 5, pp. 1128–1133, May 1987.
[22] G. Marshall and P. Mocskos, "Growth model for ramified electrochemical deposition in the presence of diffusion, migration, and electroconvection," *Phys. Rev. E*, vol. 55, no. 1, pp. 549–563, 1997.
[23] S. Ferreira, Jr., M. Martins, and M. Vilela, "Reaction–diffusion model for the growth of avascular tumor," *Phys. Rev. E*, vol. 65, no. 2, pp. 021907-1–021907-8, 2002.
[24] M. Chaplain and H. Byrne, "Mathematical models for tumour angiogenesis: Numerical simulations and nonlinear wave solutions," *Bull. Math. Biol.*, vol. 57, pp. 461–486, 1995.
[25] H. Lodish, A. Berk, P. Matsudaira, C. Kaiser, M. Krieger, M. Scott, S. Zipursky, and J. Darnell, *Molecular Cell Biology*, 5th ed. San Francisco, CA: Freeman, 2003.
[26] B. Hille, *Ion Channels of Excitable Membranes*, 3rd ed. Sunderland, MA: Sinauer Associates, 2001.
[27] P. Czapski, C. Ramon, L. Huntsman, G. Bardy, and Y. Kim, "Effects of tissue conductivity variations on the cardiac magnetic fields simulated with a realistic heart–torso model," *Phys. Med. Biol.*, vol. 41, pp. 1247–1263, 1996.
[28] A. Deutsch, S. Dormann, and P. Maini, *Cellular Automaton Modeling of Biological Pattern Formation*, 1st ed. Cambridge, MA: Birkhäuser Boston, 2004, ch. 4.
[29] A. Patel, E. Gawlinskia, S. Lemiexue, and R. Gatenbyb, "Cellular automaton model of early tumor growth and invasion: The effects of native tissue vascularity and increased anaerobic tumor metabolism," *J. Theor. Biol.*, vol. 213, pp. 315–331, 2001.
[30] F. Dorr, "The direct solution of the discrete Poisson equation on a rectangle," *SIAM Rev.*, vol. 12, no. 2, pp. 248–263, Apr. 1970.
[31] V. Lew and R. Bookchin, "Volume, pH, and ion-content regulation in human red cells: Analysis of transient behavior with an integrated model," *J. Membr. Biol.*, vol. 92, pp. 57–74, 1986.

Ahmed M. Hassan (S'07) received the B.Sc. (with highest honors) and M.Sc. degrees in electronics and communications engineering from Cairo University, Cairo, Egypt, in 2004 and 2006, respectively. He is currently working toward the Ph.D. degree at the Department of Electrical Engineering, University of Arkansas, Fayetteville.

From 2004 to 2006, he was a Teaching Assistant at Cairo University, where he was also an Assistant Lecturer during 2006. Since 2007, he has been a Teaching and Research Assistant in the Department of Electrical Engineering, University of Arkansas. His current research interests include bioelectromagnetics, modeling of the electrical activities of cancerous cells, biophysics, metamaterials, and experimental microwave imaging.

Mr. Hassan is a member of the Phi Kappa Phi Honor Society.

Magda El-Shenawee (S'90–M'91–SM'02) received the B.S. and M.S. degrees in electrical engineering from Assiut University, Assiut, Egypt, in 1976 and 1981, respectively, and the Ph.D. degree in electrical engineering from the University of Nebraska, Lincoln, in 1991.

During 1992, she was a Research Associate in the Center for Electro-Optics, University of Nebraska, where she was engaged in the problem of enhanced backscatter phenomena. During 1994, she was a Research Associate at the National Research Center, Cairo, Egypt. During 1997, she was a Visiting Scholar at the University of Illinois at Urbana-Champaign. During 1999, she was with the Multidisciplinary University Research Initiative (MURI) Team, Northeastern University, Boston, MA. She is currently an Associate Professor in the Department of Electrical Engineering, University of Arkansas, Fayetteville. Her current research interests include microwave imaging of breast cancer, computational inverse problems, microwave imaging systems, mathematical biology of breast tumors, microelectromechanical systems (MEMS) antennas, biophysics of tumors, rough surface scattering, computational electromagnetics, subsurface sensing of buried objects, landmine detection, and numerical methods for microstrip circuits.

Dr. El-Shenawee is a member of Eta Kappa Nu Electrical Engineering Honor Society.